Computers in Biology and Medicine 176 (2024) 108552

Contents lists available at ScienceDirect

Computers in Biology and Medicine

journal homepage: www.elsevier.com/locate/compbiomed

On the role of aortic valve architecture for physiological hemodynamics and valve replacement, Part II: Spectral analysis and anisotropy

Pascal Corso *, Dominik Obrist

ARTORG Center for Biomedical Engineering Research, University of Bern, Bern, Switzerland

ARTICLE INFO

Keywords:
Aortic stenosis
Bioprosthetic aortic valve replacement
Flow turbulence
Helicity
Kinetic energy anisotropy
Spectral analysis

ABSTRACT

Severe aortic valve stenosis can lead to heart failure and aortic valve replacement (AVR) is the primary treatment. However, increasing prevalence of aortic stenosis cases reveal limitations in current replacement options, necessitating improved prosthetic aortic valves. We investigate flow disturbances downstream of severe aortic stenosis and two bioprosthetic aortic valve (BioAV) designs using advanced energy-based analyses. Three-dimensional high-fidelity fluid–structure interaction simulations have been conducted and a dedicated and novel spectral analysis has been developed to characterise the kinetic energy (KE) carried by eddies in the wavenumber space. In addition, new field quantities, i.e. modal KE anisotropy intensity as well as normalised helicity intensity, are introduced. Spectral analysis shows kinetic energy (KE) decay variations, with the stenotic case aligning with Kolmogorov's theory, while BioAV cases differing. We explore the impact of flow helicity on KE transfer and decay in BioAVs. Probability distributions of modal KE anisotropy unveil flow asymmetries in the stenotic and one BioAV cases. Moreover, an inverse correlation between temporally averaged modal KE anisotropy and normalised instantaneous helicity intensity is noted, with the coefficient of determination varying among the valve configurations. Leaflet dynamics analysis highlights a stronger correlation between flow and biomechanical KE anisotropy in one BioAV due to higher leaflet displacement magnitude. These findings emphasise the role of valve architecture in aortic turbulence as well as its importance for BioAV performance and energy-based design enhancement.

1. Introduction

Calcific aortic valve stenosis is characterised by a progressive deterioration, remodelling and thickening of the native aortic valve leaflet tissue, causing a reduction in its functional flexibility [1]. This condition, referred to as aortic stenosis (AS), results in increased resistance to blood flow from the left ventricle to the aorta, particularly during systole and the potential for blood regurgitation during diastole [2–4]. Aortic valve stenotic disease is the most commonly occurring valvular pathology in developed countries (afflicting 9 million people worldwide) and its prevalence has been increasing with population ageing [5]. Moreover, surgical aortic valve replacements tally around 300,000 cases annually and this number is projected to double by 2050 due to the ageing global population [6]. The long-term implications of this pathology are serious. The AS is generally defined as severe when a significant left ventricular outflow tract (LVOT) obstruction is present, leading to a reduced orifice area and high downstream jet velocity, and when symptoms such as dyspnea, heart failure, chest pain or syncope appear [7]. To address this critical issue, the replacement with valvular prostheses has emerged as a prevalent solution. These prostheses come in two primary types: mechanical heart valves made from rigid materials such as titanium or carbon and bioprosthetic or tissue aortic valves (BioAVs) manufactured based on biological tissue. The replacement of the diseased native aortic valve is achieved through a medical procedure known as aortic valve replacement (AVR).

Previous studies have extensively explored the haemodynamic performance of aortic valves made from biological materials like porcine or bovine pericardium [2,4,8–12]. However, the correlation between the kinetic energy (KE) present within the valve components (i.e. leaflets and supporting ring) and the energy carried by the turbulent structures in the flow surrounding the BioAV has yet to be investigated, either *in vitro* or *in silico*. Becsek et al. [9] presented a computational characterisation of the turbulent features of the flow downstream of one bioprosthetic aortic valve model under peak systolic conditions. One-dimensional wavenumber energy spectra were calculated at various distances from the sino-tubular junction and it was argued that the spectra based on points diametrically aligned where the turbulent dissipation rate is the largest could be connected to shear-induced thrombocyte activation. Finally, it was noticed that the presence of

* Correspondence to: Freiburgstrasse 3, 3010 Bern, Switzerland.
E-mail address: pascal.corso@unibe.ch (P. Corso).

https://doi.org/10.1016/j.compbiomed.2024.108552
Received 20 November 2023; Received in revised form 14 April 2024; Accepted 29 April 2024
Available online 3 May 2024

zones with elevated and fluctuating wall shear stress at the aortic wall that could possibly underline the presence of endothelial lesions in these zones. Nonetheless, the wavenumber kinetic energy spectra considered in Becsek et al. [9] were one-dimensional and limited to a confined region of the flow along a line perpendicular to the centreline, thus excluding the study of anisotropy in the kinetic energy (KE). Besides, in Corso et al. [2,3,13], similar conclusions were drawn using both *in vitro* three-dimensional particle tracking velocimetry experiments and data from direct numerical simulation downstream of a stenotic aortic valve. The detrimental effect of turbulence on blood platelet damage and on the production of important irreversible pressure loss due to elevated haemodynamic turbulent stresses was assessed. Moreover, it was emphasised that considering Reynolds' stress close to the wall is crucial for accurately evaluating wall shear stress from flow field data when dealing with limited spatial resolution, especially in the case of disturbed aortic flows. Recently, Gallo et al. [10] explored the relationship between phase-averaged and fluctuating helicity as well as phase-averaged and turbulent kinetic energy, for both a mechanical heart valve and a bioprosthetic heart valve. To this end, they simulated the coupled fluid–structure interaction problem by applying the interface conditions through an immersed body surface method using a moving least square algorithm for the interpolation and spreading of the information between the Lagrangian and Eulerian discretisation points. A Navier–Stokes flow solver together with two simplified solid motion solver, one for the rigid mechanical valve and one mass–spring model for the bioprosthetic valve with elastic leaflets, were employed. The study showed that the haemodynamics downstream of the mechanical valve exhibited larger phase-averaged and fluctuating helicity compared to that downstream of the bioprosthetic valve. For both heart valve types, strong linear correlations were found between volume-averaged kinetic energy and helicity when considering phase-averaged or fluctuating quantities. Peaks of turbulent kinetic energy (TKE) or fluctuating helicity for both heart valve types was delayed as compared to the peaks of mean kinetic energy and phase-averaged helicity. While this study introduces novelty in exploring the relationship between flow helicity and kinetic energy and utilises data from 20 simulated cardiac cycles to compute flow field statistics, there are several areas that can be improved. These pertain to the use of a simplified mass–spring model to solve the dynamics of the deformable leaflets, the assumption of a rigid aortic wall and the absence of a ring supporting the valve leaflets in the simulations. Furthermore, an in-depth examination of the spatial distribution of kinetic energy, helicity and their relationship to leaflets and valve designs was not conducted.

The present work is the second part of a comprehensive two-part study. Both parts utilise validated and high-fidelity computational approaches. In this paper, the analysis strives to comprehensively characterise the turbulence by inspecting the energy carried by the vortical structures of the flow following vortex ring formation, a shedding process including vortex stretching and advection [14]. We seek to observe the typical energy decay of kinetic energy (KE), as described in the theory of turbulence [15]. Additionally, we investigate any deviations from this theoretical energy decay along with examining the dissipation rate of KE. Connection between leaflet geometries and turbulence characteristics is underlined. In addition, we analyse and correlate the spatial distributions of the newly introduced concepts of kinetic energy anisotropy and helicity intensity over spherical shells close to the valvular orifice. There has been no previous computational study and comprehensive energy-based analyses that include valve bioprostheses of different designs alongside a comparative assessment with a severe stenotic case. This work significantly contributes to the development of optimally designed valves by thoroughly elucidating the flow-energy-based mechanisms downstream of BioAVs in comparison to those encountered downstream of a severe aortic stenosis.

2. Methods

2.1. Numerical models

For detailed information on the geometry of the aortic model, the two valvular bioprostheses, and aortic stenosis, as well as details about the numerical setups, solving methods, and experimental validation of the solvers, readers are referred to the first part of the present extensive study [14] as well as three works by Corso et al. [2,3,13] for the stenotic case. The following paragraphs provide the reader with a summary of the numerical experiments implemented. In the case of the severely calcified valve, the leaflets are considered immobile due to extensive calcification deposited onto a tricuspid aortic valve. The geometries of the curved aorta and stenotic orifice are patient-specific and were obtained from high-resolution phase-contrast magnetic resonance imaging [2,3,13] (see Fig. S3 (a-c) in the supporting information (SI)). The open-source spectral element solver, NEK5000 [16], is used to fully resolve the incompressible Navier–Stokes equations in the stenosed aorta geometry. For this purpose, a mesh skeleton consisting of 92,208 conforming curved-sided hexahedral elements is generated and the pressure and velocity fields are resolved by expressing them over each spectral element using a 7th order polynomial. A third-order accurate temporal integration scheme is employed, with a constant time-step equal to 1.54 μs corresponding to a non-dimensional time-step of 10^{-4} [3]. The walls of the stenosed aorta are assumed rigid and the simulated flow conditions are systolic. This is ensured by imposing velocities at the inflow cross-section located at the corresponding left ventricular outflow tract (LVOT). The mean Reynolds number at the stenotic orifice is equal to 3,800 [3,14].

In regard to the simulation of coupled biological valve motion and blood dynamics, the geometries of the two tested BioAVs are depicted in Fig. S3 (d, e, g, h) of the SI. The various geometrical parameters for the 500-micron-thick leaflet shape can be categorised based on three main features [14,17]: (i) the belly curve, obtained by longitudinally cutting the leaflet in half; (ii) the attachment or scallop curve, representing the leaflet extremity attached to the ring; and (iii) the free edge, denoting the leaflet extremity not attached to the ring (see Fig. S3 (d, e, g, h) of the SI). Further information on the parametrisation of these three geometrical features, aimed at modifying valve leaflet design, can be found in the first part of the study [14]. The computational domain comprises a rectilinear grid with periodic boundary conditions for the fluid sub-problem in all three directions and embedded structures including the aortic root, the ascending aorta and the flexible aortic valve model (cf. Fig. S3 (f, i) of the SI). The proposed numerical experiments on the BioAV cases employ a fluid–structure interaction (FSI) solving algorithm [18]. This algorithm couples a fluid sub-problem solved using a sixth-order finite-difference formulation with a solid sub-problem solved using a finite-element formulation. Unlike classical immersed boundary methods [19], the transfer of fluid velocities to the structure and reaction forces from the structure to the fluid is performed along the shared interface by means of L^2-projections, hence the term *variational transfer* [18]. This transfer of information ensures velocity and force continuity at the fluid-solid interface. The fluid and solid sub-problems are solved synchronously with a time-step of 5 μs. Regarding the material properties for the structural parts of the studied FSI problems, a fibre-reinforced material model is employed to characterise the anisotropic material properties of the leaflets [20]. This six-parameter constitutive relation models the presence of two families of collagen fibres oriented at a fitted angle of 60° to each other. The parameters of the anisotropic constitutive law were fitted to match bi-axial tensile tests performed on glutaraldehyde-fixed bovine pericardium tissue [21]. The material properties of the aortic wall and the supporting ring of the leaflets are described by an isotropic linear elastic material model (density of the valve ring $\rho_r = 1500\ \mathrm{kg/m^3}$; density of the leaflets, aortic root, and aorta $\rho_l = \rho_S = \rho_{Ao} = 1100\ \mathrm{kg/m^3}$, bulk modulus: 3 MPa and shear modulus: 0.3

MPa for all solid parts). Blood is approximated as an incompressible, homogeneous and Newtonian fluid (density $\rho = 1060\ \mathrm{kg/m^3}$, dynamic viscosity $\mu = 0.004$ Pa.s) [11,14]. To impose systolic flow conditions in the fluid domain discretised by a rectilinear grid of points set with periodic conditions at its borders, a forcing term is added to the right-hand side of the Navier–Stokes momentum equation [14]. Cylindrical fringe regions of the fluid grid are defined to impose a prescribed pressure difference at inflow and outflow regions [14] (cf. Fig. S3 (i) of the SI). This results in the imposition of an accelerating and decelerating inflow rate corresponding to a Reynolds number averaged over systole of 3,800 (see SI of the first part of the study [14]).

2.2. Spectral analysis on the blood motion

The spectral analysis proposed in this study relies upon the incompressible Navier–Stokes equations expressed in Fourier space [22]:

$$\boldsymbol{\kappa} \cdot \hat{\mathbf{u}}(\boldsymbol{\kappa}) = 0, \tag{1}$$

$$\frac{d\hat{\mathbf{u}}(\boldsymbol{\kappa})}{dt} + i \sum_{\boldsymbol{\kappa}'} \{\boldsymbol{\kappa} \cdot \hat{\mathbf{u}}(\boldsymbol{\kappa} - \boldsymbol{\kappa}')\}\hat{\mathbf{u}}(\boldsymbol{\kappa}') = -i\boldsymbol{\kappa}\, \hat{p}(\boldsymbol{\kappa}) - \nu\kappa^2 \hat{\mathbf{u}}(\kappa), \tag{2}$$

with $\boldsymbol{\kappa}$, the angular wavenumber vector; $\mathbf{u}$, the instantaneous flow velocity vector; $\hat{\mathbf{u}}$, the Fourier modes of $\mathbf{u}$; $i = \sqrt{-1}$; ν, the kinematic viscosity and $\hat{p}(\boldsymbol{\kappa})$, the modal kinematic pressure.

From these spectral equations, after eliminating the pressure term by projecting the advective term on the space of incompressibility [23], an equation describing the dynamics of the modal kinetic energy $\hat{E}_{u^2}$ can be derived by taking the inner product of Eq. (2) with the complex conjugate $\hat{\mathbf{u}}^*(\kappa)$ and adding the complex conjugate to the resulting equation. We obtain the following equation [15,22]:

$$\frac{d}{dt}\hat{E}_{u^2}(\boldsymbol{\kappa}) = \underbrace{\sum_{\boldsymbol{\kappa}'} \Im\mathfrak{m}\left(\{\boldsymbol{\kappa} \cdot \hat{\mathbf{u}}(\boldsymbol{\kappa} - \boldsymbol{\kappa}')\}\{\hat{\mathbf{u}}(\boldsymbol{\kappa}') \cdot \hat{\mathbf{u}}^*(\boldsymbol{\kappa})\}\right)}_{\hat{T}_{u^2}(\boldsymbol{\kappa})} - \underbrace{2\nu\kappa^2 \hat{E}_{u^2}(\boldsymbol{\kappa})}_{\hat{D}_{u^2}(\boldsymbol{\kappa})}, \tag{3}$$

with $\hat{E}_{u^2}$, the modal kinetic energy; $\hat{T}_{u^2}$, the rate of kinetic energy transfer to the modal kinetic energy due to non-linearity and $\hat{D}_{u^2}$, the dissipation rate of modal kinetic energy through viscous effects. $\Im\mathfrak{m}$ is the imaginary part.

It is possible to calculate the total dissipation rate ε by summing $\hat{D}_{u^2}(\boldsymbol{\kappa})$ over the wavenumber. This dissipation ε is used to estimate the Kolmogorov microscales [15]. Furthermore, it is suggested in [24] that for non-isotropic turbulence, the spatial velocity function and the spectrum function be expressed in terms of a single scalar distance r and wavenumber κ, respectively, by taking mean values of the functions over spherical surfaces given by radius r = constant in physical space and κ = constant in Fourier space. This way, the kinetic energy of the Fourier modes $\hat{E}_{u^2}$ of the three-dimensional and anisotropic velocity field obtained from the simulations is calculated by sampling the velocity components on points distributed over spherical shells centred around a point on the centreline of the ascending aorta (see Fig. 1). A sequence of velocity values ($\mathbf{u}_s$) is then defined over each radius of the sphere of points. The points on each spherical shell (i.e. at r = constant) are obtained by distributing them with a constant increment in both azimuthal and elevation angles of 30 degrees, resulting in a set of 122 equidistant points on the shell, spaced at an arc length of $\frac{\pi r}{6}$.

A one-dimensional continuous Fourier transform operator on a finite interval $(0, \mathcal{L})$ allowing to express the Fourier coefficients of the continuous three-dimensional velocity field $\mathbf{u}(\boldsymbol{x})$ is defined as follows [15]:

$$\mathcal{F}_\kappa\{\mathbf{u}(r)\} = \hat{\mathbf{u}}(\kappa) = \frac{1}{\mathcal{L}} \int_0^{\mathcal{L}} \mathbf{u}(r) \exp(-i\kappa r)\, dr, \tag{4}$$

with r, the radial coordinate along each radius of the sphere of points; $\mathcal{L}$, the radius of the largest spherical surface used for the sampling. The largest radius is equal to 10 mm and 11.5 mm for the aortic stenosis and bioprosthesis cases, respectively. The three-dimensional formulation of the Fourier operator is reduced to the above one-dimensional formulation by integrating along each radius of the sphere of points and by considering $\boldsymbol{\kappa} \cdot \boldsymbol{x} = \kappa r$ [15].

The corresponding discrete Fourier transform (DFT) using a fast Fourier transform (FFT) algorithm [26] is performed based on the instantaneous velocity field $\mathbf{u}$ sampled on a sequence of points distributed over spherical shells ($\mathbf{u}_s$) as shown in Fig. 1. It is important to note that the calculation of discrete Fourier modes implies the periodicity in the sampled velocity field $\mathbf{u}_s$. However, if we consider the integral length scale $\mathfrak{L}$, the effects of this artificially imposed periodicity vanish as $\frac{\mathcal{L}}{\mathfrak{L}}$ tends to infinity [15]. The centre of the spherical shells is positioned on the centreline of the straight aorta at a distance of 12.5 mm and 8 mm from the sino-tubular junction in the stenotic and BioAV cases, respectively. The DFT is then expressed as:

$$\hat{\mathbf{u}}_k = \frac{1}{(N-1)\Delta r} \sum_{s=0}^{N-1} \mathbf{u}_s \exp\left(\frac{-i2\pi ks}{N}\right) \Delta r, \tag{5}$$

with $k = 0, \ldots, N-1$. N is the number of points taken over each radius of the spherical distribution of points. N is equal to 82 and 48 for the stenotic and BioAV cases, respectively. Δr is the distance between two consecutive spherical shells and is equal to 125 μm for the stenosis case and 250 μm for the aortic bioprosthesis cases. Each entry of the sequence of scalar angular wavenumbers κ corresponding to the sequence $(\hat{\mathbf{u}}_k)$ is $\kappa_k = \frac{(k+1)}{N}\frac{2\pi}{\Delta r}$ leading to $\hat{\mathbf{u}}(\kappa) = \hat{\mathbf{u}}_k$.

In order to avoid the presence of aliases in the spectrum obtained out of the FFT operation and considering the symmetry of the spectrum given the real-valued velocity sequence ($\mathbf{u}_s$), the values of $\hat{\mathbf{u}}(\kappa)$ above the folding wavenumber $\kappa_f = \frac{\pi}{\Delta r}$ are discarded. These correspond to the entries $\hat{\mathbf{u}}_k$ with index $k > \lfloor\frac{N+1}{2}\rfloor = N'$. The normalised and discrete first-order autocorrelation function over each radius of the spherical distribution of points is then calculated from the modal velocity vector $\hat{\mathbf{u}}_k(\hat{u_{x\,k}}, \hat{u_{y\,k}}, \hat{u_{z\,k}})$:

$$\hat{\mathcal{R}}_I^{u_j u_j} = \frac{1}{|\hat{\mathcal{R}}_0^{u_j u_j}|} \sum_{n=0}^{N'-m-1} \left(\hat{u}_{j\,n+I}\, \hat{u}^*_{j\,n}\right), \tag{6}$$

with $j = (x, y, z)$, $m = 1, \ldots, 2N'-1$, the index $I \in [-N', N']$ and the range of indices I considered for $\hat{\mathcal{R}}^{u_i u_i}$ is $[0, N']$. By inspecting the distribution of the correlation function over the points of each spherical shell, we note a log-normal distribution. Therefore, in order to have the most representative value of the autocorrelation function $\hat{\mathcal{R}}^{u_j u_j}$ over each spherical surface, the mode of this distribution instead of the previously mentioned expected value [24] has been employed to compute an equivalent autocorrelation function $\hat{\mathcal{R}}^{u_j u_j}$ so that the latter is dependent on a single scalar wavenumber κ for each spherical shell. The equivalent correlation function (coming from the mode of the log-normal distribution) is then defined as:

$$\hat{\mathcal{R}}^{u_j u_j}\Big|_{\mathrm{eq}} = \exp(M^{\mathcal{R}} - \Sigma^{\mathcal{R}}), \tag{7}$$

$M^{\mathcal{R}} = \log\left[\frac{\langle\hat{\mathcal{R}}^{u_j u_j}|_{\mathrm{sph}}\rangle}{\sqrt{\langle\hat{\mathcal{R}}^{u_j u_j}|_{\mathrm{sph}}\rangle^2 + \mu_2(\hat{\mathcal{R}}^{u_j u_j}|_{\mathrm{sph}})}}\right]$, $\Sigma^{\mathcal{R}} = \log\left[1 + \frac{\mu_2(\hat{\mathcal{R}}^{u_j u_j}|_{\mathrm{sph}})}{\langle\hat{\mathcal{R}}^{u_j u_j}|_{\mathrm{sph}}\rangle^2}\right]$, with $\langle\hat{\mathcal{R}}^{u_j u_j}|_{\mathrm{sph}}\rangle$; the expected value and $\mu_2(\hat{\mathcal{R}}^{u_j u_j}|_{\mathrm{sph}})$; the variance of $\hat{\mathcal{R}}^{u_j u_j}$ over the 122 points of each spherical shell.

Finally, each term of Eq. (3) is calculated based on the one-dimensional DFT of the velocity field sampled on points distributed over spherical shells and based on the ensuing equivalent autocorrelation function $\hat{\mathcal{R}}^{u_j u_j}\Big|_{\mathrm{eq}}$. Therefore, the equivalent modal KE, $\hat{E}_{u^2}(\kappa)$, reads:

$$\hat{E}_{u^2}(\kappa) = \frac{1}{2}\left(\hat{\mathcal{R}}^{u_x u_x}\Big|_{\mathrm{eq}} + \hat{\mathcal{R}}^{u_y u_y}\Big|_{\mathrm{eq}} + \hat{\mathcal{R}}^{u_z u_z}\Big|_{\mathrm{eq}}\right). \tag{8}$$

In the main body of the paper, the circumflex accent is omitted to indicate the modal kinetic energy, i.e. $E_{u^2}(\kappa)$.

The rate of modal KE transfer $\hat{T}_{u^2}(\kappa)$ is computed as follows:

$$\hat{T}_{u^2}(\kappa) = \frac{1}{2}\left(\hat{T}^{u_x^2}\Big|_{\mathrm{eq}} + \hat{T}^{u_y^2}\Big|_{\mathrm{eq}} + \hat{T}^{u_z^2}\Big|_{\mathrm{eq}}\right), \tag{9}$$

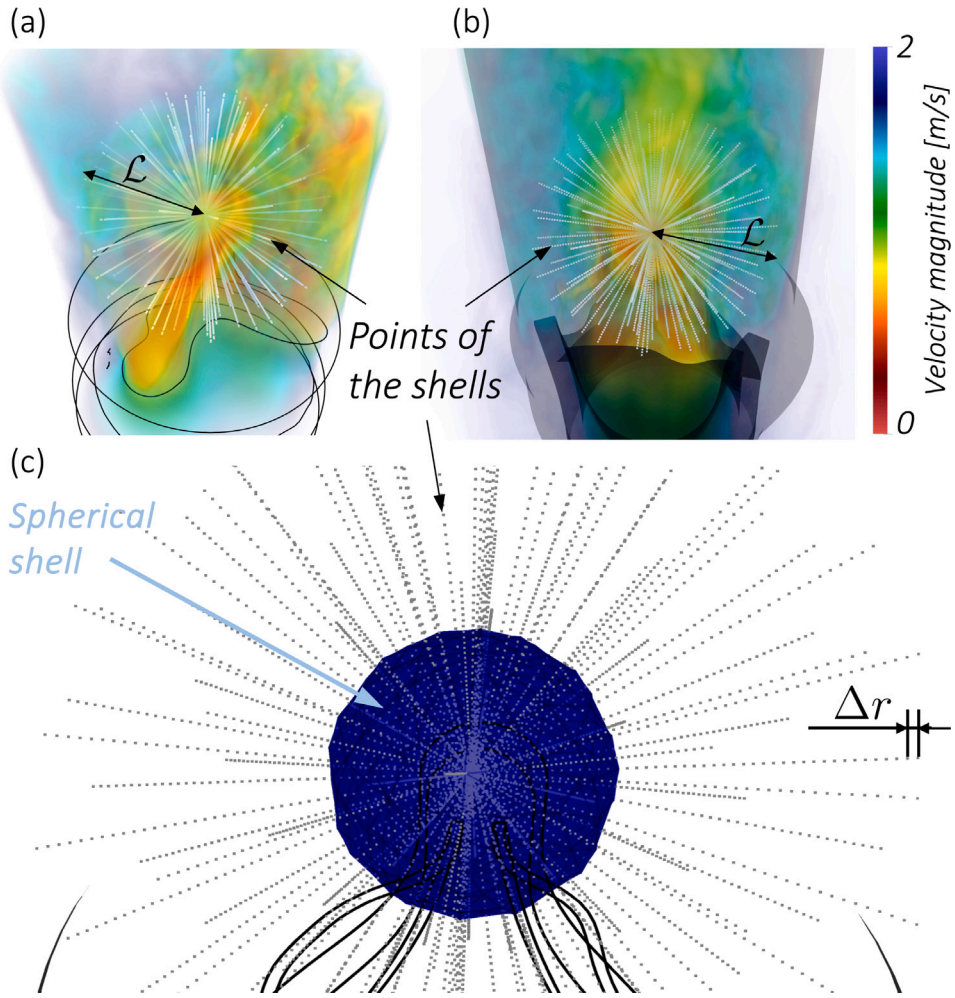

Fig. 1. Definition of the points on spherical shells for the computation of the Fourier modes and of the first-order autocorrelation function as part of the spectral analysis for (a) the stenotic case and (b) one of the BioAV cases (VLth30). The spherical surface consists of 122 points as displayed in (c) equally spaced by a distance Δr of 125 μm in the stenotic case and 250 μm in the BioAV cases. The largest radius $\mathcal{L}$ for the spherical shell is equal to 10 mm and 11.5 mm for the stenotic and BioAV cases, respectively. The centre of the spheres is on the centreline of the straight ascending aorta. The instantaneous velocity magnitude is visualised in (a) and (b) through volumetric rendering [25] displaying the jet of high velocity issuing from the valvular orifice.

where

$$\hat{T}^{u_j^2}(\kappa) = \sum_{\kappa'} \Im\mathfrak{m}\left(\{\kappa \cdot \hat{u_j}(\kappa - \kappa')\}\{\hat{u_j}(\kappa') \cdot \hat{u_j}^*(\kappa)\}\right), \tag{10}$$

and

$$\hat{T}^{u_j^2}\Big|_{\text{eq}} = \exp(M^T - \Sigma^T), \tag{11}$$

$$\text{with } M^T = \log\left[\frac{\langle \hat{T}^{u_j^2}|_{\text{sph}}\rangle}{\sqrt{\langle \hat{T}^{u_j^2}|_{\text{sph}}\rangle^2 + \mu_2(\hat{T}^{u_j^2}|_{\text{sph}})}}\right],\ \Sigma^T = \log\left[1 + \frac{\mu_2(\hat{T}^{u_j^2}|_{\text{sph}})}{\langle \hat{T}^{u_j^2}|_{\text{sph}}\rangle^2}\right].$$

2.3. Kinetic energy, enstrophy and helicity in blood flow

To obtain the fluctuations in the velocity $\mathbf{u}'$ and vorticity $\boldsymbol{\omega}'$ fields of blood flow, a Reynolds decomposition is performed. With a view of removing the effect of the temporal periodicity in the leaflet motion on the downstream flow, the time-averaged (over all the considered time-steps) velocity and vorticity fields are combined with the velocity and vorticity field phase-averaged at the main frequencies extracted from the leaflet motion analysis [14]. This decomposition is akin to performing a triple decomposition [12,27] and leads to the following formulation for the fluctuating vector fields:

$$\begin{aligned}\mathbf{u}' &= \mathbf{u} - \frac{1}{2}\mathbf{U} - \frac{1}{2}\mathbf{U}_{\text{periodic}} \\ &= \mathbf{u} - \underbrace{\frac{1}{2}\left[\frac{1}{T}\int_0^T \mathbf{u}\, dt + \frac{1}{N}\sum_N \mathbf{u}(t + \frac{N}{f_{\text{mech}}})\right]}_{\mathbf{U}^{\text{tot}}},\end{aligned} \tag{12}$$

with $\mathbf{U}$, the velocity vector field averaged over the whole simulated systole T; $\mathbf{U}_{\text{periodic}}$, the phase-averaged velocity field at frequencies f_{mech} evaluated from the leaflet mechanics characterisation [14]. The average between these two time-averaged velocity fields gives $\mathbf{U}^{\text{tot}}$.

Likewise, the fluctuating vorticity field is given by:

$$\begin{aligned}\boldsymbol{\omega}' &= \boldsymbol{\omega} - \frac{1}{2}\boldsymbol{\Omega} - \frac{1}{2}\boldsymbol{\Omega}_{\text{periodic}} \\ &= \boldsymbol{\omega} - \underbrace{\frac{1}{2}\left[\frac{1}{T}\int_0^T \boldsymbol{\omega}\, dt + \frac{1}{N}\sum_N \boldsymbol{\omega}(t + \frac{N}{f_{\text{mech}}})\right]}_{\boldsymbol{\Omega}^{\text{tot}}},\end{aligned} \tag{13}$$

with $\boldsymbol{\omega} = \nabla \times \mathbf{u}$, the instantaneous vorticity field; $\boldsymbol{\Omega}$, the mean vorticity vector field time-averaged over the whole systole, $\boldsymbol{\Omega}_{\text{periodic}}$, the vorticity field phase-averaged at frequencies evaluated from the leaflet mechanics characterisation [14] and $\boldsymbol{\Omega}^{\text{tot}}$, the arithmetic average of the latter two vorticity fields averaged in time. The terms accounting

for the periodicity in the flow field due to the periodic leaflet motion ($\mathbf{U}_{\text{periodic}}$ and $\boldsymbol{\Omega}_{\text{periodic}}$) are obviously null in the stenotic case and in the case where the leaflets are not moving.

The total turbulent KE, fluctuating enstrophy and fluctuating helicity are given by:

$$TE_{u'^2} = \int_r \frac{1}{2}\left(\mathbf{u}'(r)\cdot\mathbf{u}'(r)\right)dr, \tag{14}$$

$$TE_{\omega'^2} = \int_r \frac{1}{2}\left(\boldsymbol{\omega}'(r)\cdot\boldsymbol{\omega}'(r)\right)dr, \tag{15}$$

$$TE_{|h'|} = \int_r \frac{1}{2}|\mathbf{u}'(r)\cdot\boldsymbol{\omega}'(r)|dr, \tag{16}$$

$$TE_{h'} = \int_r \frac{1}{2}\left(\mathbf{u}'(r)\cdot\boldsymbol{\omega}'(r)\right)dr, \tag{17}$$

with r, the coordinate along each radius corresponding to the radius from the centre point of the spherical distribution of points defined in the spectral analysis section.

The mean KE, enstrophy and helicity are defined as:

$$TE_{U^2} = \int_r \frac{1}{2}\left(\mathbf{U}^{\text{tot}}(r)\cdot\mathbf{U}^{\text{tot}}(r)\right)dr, \tag{18}$$

$$TE_{\Omega^2} = \int_r \frac{1}{2}\left(\boldsymbol{\Omega}^{\text{tot}}(r)\cdot\boldsymbol{\Omega}^{\text{tot}}(r)\right)dr, \tag{19}$$

$$TE_{|H|} = \int_r \frac{1}{2}|\mathbf{U}^{\text{tot}}(r)\cdot\boldsymbol{\Omega}^{\text{tot}}(r)|dr, \tag{20}$$

$$TE_{H} = \int_r \frac{1}{2}\left(\mathbf{U}^{\text{tot}}(r)\cdot\boldsymbol{\Omega}^{\text{tot}}(r)\right)dr. \tag{21}$$

The turbulence intensity $\mathbb{I}_{u'^2}$ (Eq. (22)), intensity of fluctuating enstrophy $\mathbb{I}_{\omega'^2}$ (Eq. (23)), intensity of unsigned fluctuating helicity $\mathbb{I}_{|h'|}$ (Eq. (24)) and intensity of signed fluctuating helicity $\mathbb{I}_{h'}$ (Eq. (25)) are calculated by taking the ratio of the aforementioned fluctuating and mean quantity fields:

$$\mathbb{I}_{u'^2} = \frac{TE_{u'^2}}{TE_{U^2}} \tag{22}$$

$$\mathbb{I}_{\omega'^2} = \frac{TE_{\omega'^2}}{TE_{\Omega^2}} \tag{23}$$

$$\mathbb{I}_{|h'|} = \frac{TE_{|h'|}}{TE_{|H|}} \tag{24}$$

$$\mathbb{I}_{h'} = \frac{TE_{h'}}{TE_{H}} \tag{25}$$

Similarly to the calculation of the equivalent autocorrelation function $\hat{\mathcal{R}}^{u_j u_j}$ and the corresponding modal KE ($\hat{E}_{u^2}$), we compute an equivalent value for the foregoing intensity fields at each time instance under consideration. This equivalent value represents the most representative intensity field value over the 122 points of the spherical shells and it is determined by taking the mode of the log-normal distribution (cf. Eq. (7)).

2.4. Flow modal kinetic energy and helicity intensity

The total flow KE ($\mathcal{K}_{p_s}$) for each point p_s of the spherical shell is calculated from the normalised and discrete first-order autocorrelation function as follows:

$$\mathcal{K}_{p_s} = \frac{1}{2}\sum_j \int_\kappa \hat{\mathcal{R}}^{u_j u_j}\Big|_{\text{sph}}\, d\kappa, \tag{26}$$

with $j = (x, y, z)$ and $p_s = 1, \ldots, 122$, which corresponds to the index of each point on the spherical shell. The numerical integration is performed using the trapezoidal rule. The flow modal KE anisotropy $\mathbb{I}_{p_s}^{\text{flow anis}}$ over a spherical region close to the aortic orifice is thus defined as:

$$\mathbb{I}_{p_s}^{\text{flow anis}} = \frac{\mathcal{K}_{p_s} - \langle\mathcal{K}_{p_s}\rangle}{\langle\mathcal{K}_{p_s}\rangle} \times 100, \tag{27}$$

with $\langle\cdot\rangle$, the average operator over the 122 points of the spherical shell.

A normalised helicity intensity $\mathbb{I}_{p_s}^{h|_{\text{sph}}}$ is computed along each radial direction of the spherical shells from the instantaneous helicity intensity field through the following equation:

$$\frac{\mathbb{I}_{p_s}^{h|_{\text{sph}}}}{100} = \frac{\int_r \frac{1}{2}\left(\mathbf{u}(r)\cdot\boldsymbol{\omega}(r)\right)\, dr}{\langle\int_r \frac{1}{2}\left(\mathbf{u}(r)\cdot\boldsymbol{\omega}(r)\right)\, dr\rangle} = \frac{TE_h\big|_{\text{sph}}}{\langle TE_h\big|_{\text{sph}}\rangle} = \frac{\mathbb{I}_h\big|_{\text{sph}}}{\langle\mathbb{I}_h\big|_{\text{sph}}\rangle}. \tag{28}$$

2.5. Anisotropy in leaflet and ring kinetic energy

The KE computed at the mesh points p_m located at the leaflet or ring interfaces of the simulated bioprosthetic valve motion is expressed as:

$$KE_{p_m}^{\text{struct}} = \frac{1}{2}\sum_j \mathrm{v}_j^2|_{\text{int}}, \tag{29}$$

with $\mathrm{v}_j|_{\text{int}}$, the j$^{\text{th}}$ velocity component of the structure at the fluid-solid interface (int), which is equal to the flow velocity at the interface by virtue of the velocity continuity condition. The KE anisotropy $\mathbb{I}_{p_m}^{\text{struct anis}}$ in the structure (ring and leaflet) is then defined as:

$$\frac{\mathbb{I}_{p_m}^{\text{struct anis}}}{100} = \left[\frac{KE_{p_m}^{\text{struct}} - \langle KE_{p_m}^{\text{struct}}\rangle}{\langle KE_{p_m}^{\text{struct}}\rangle}\right]\left(\mathbf{p}^{\text{struct}}\cdot\mathbf{n}^{\text{struct}}\right), \tag{30}$$

with $\mathbf{p}^{\text{struct}}$, the coordinates of tetrahedral mesh points of the considered structure (leaflet or ring) and $\mathbf{n}^{\text{struct}}$, the outward normal vector to the considered mesh point of the structure. The operator $\langle\cdot\rangle$ corresponds to the average over the different mesh points of the structure.

3. Results and discussion

3.1. Spectral analysis and turbulence characteristics

The log–log graphs presented in Fig. 2 (a, b, c) display the distribution of the modal KE (E_{u^2}), as defined in Eq. (8), at different scalar angular wavenumbers κ for various time instances considered over systole, represented by thin grey lines. Details on the geometry of three valvular configurations, the stenosed aorta case and the two newly designed bioprosthetic valves (VLth30 and Ulth0), are presented in the Methods section of the present article and in the first part of the study [14]. In the stenotic case, we note that the trend in the decay of energy as a function of the wavenumber varies depending on the time instant considered as shown by the large difference in E_{u^2} between the dash–dot black line and the solid thick black line, especially for wavenumbers larger than 2,000 rad/m. The maximum non-dimensional modal KE curve (i.e. solid thick line in Fig. 2 (a)) corresponds to the wavenumber spectra at instants t = 0.121 s, 0.142 s and 0.172 s. The minimum non-dimensional modal KE curve (cf. dash–dot line in Fig. 2 (a)) corresponds to the spectra at t = 0.1 s. Concerning the VLth30 BioAV case, the log–log plot (see Fig. 2 (b)) shows that the variations in the energy decay over the different time instants is smaller than that noted in the stenotic case. These differences between time instances in E_{u^2} are even smaller in the Ulth0 BioAV case. Indeed, as presented in the first part of the study [14], the Ulth0 valve design leads to very limited leaflet motion after their opening throughout systole and the jet shape downstream remains relatively stable, except for Kelvin–Helmholtz instability (KHI) arising between t = 0.12 s and t = 0.21 s.

In order to verify whether the algebraic decay of −5/3 characteristic of the inertial subrange for turbulent flows according to Kolmogorov's theory [15] can be noted, E_{u^2} has been divided by $\kappa^{-5/3}\varepsilon^{2/3}$ and the graphs of the first-order derivative with respect to the wavenumber are presented in Fig. 2 (d, e, g). Additionally, the temporal evolution of the turbulent KE dissipation ε is presented in Fig. 3 (b). For the stenosed aorta case, the curves of minimum, median and maximum non-dimensional $d\left(\frac{E_{u^2}}{\kappa^{-5/3}\varepsilon^{2/3}}\right)/d\kappa$ are almost superimposed on each other. Moreover, these curves follow the universal scaling law predicted

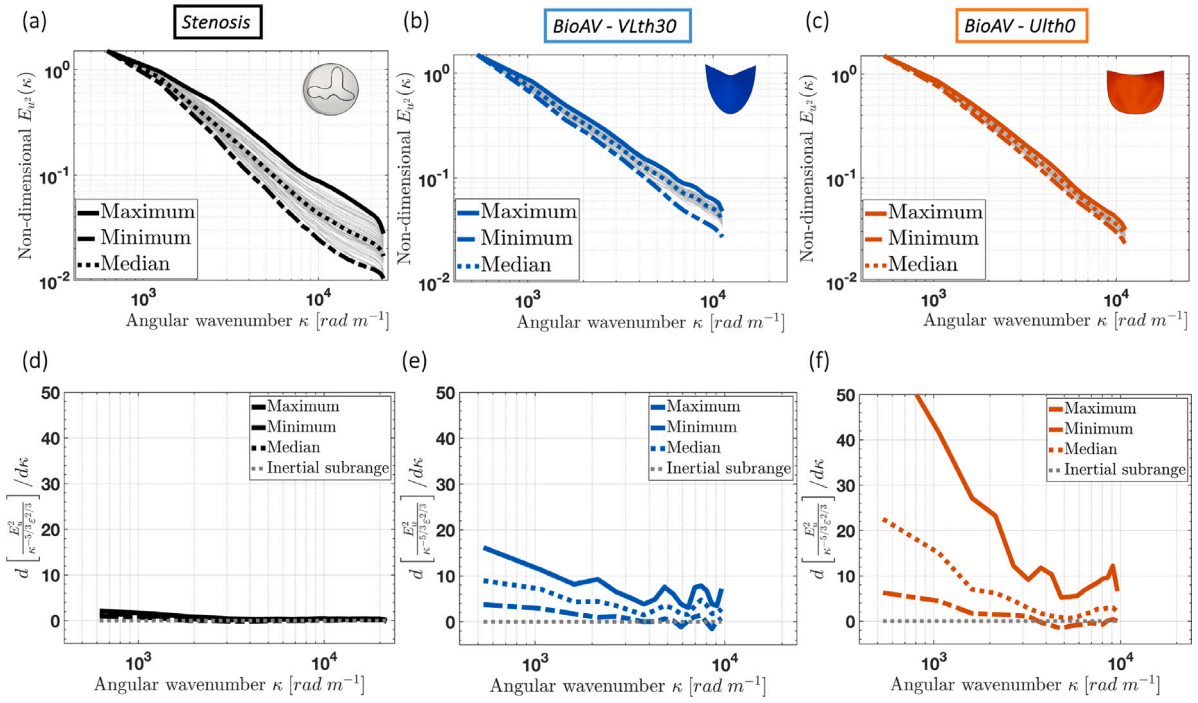

Fig. 2. Three-dimensional wavenumber spectra of kinetic energy for the three valvular cases are shown in (a), (b) and (c). These spectra represent the spectral curve for all the considered time instances between t = 0.1 and t = 0.3 s, highlighting the maximum, minimum, and median values at each scalar wavenumber. (d), (e), and (f) display the derivative of the modal KE with respect to the angular wavenumber to determine whether the well-known −5/3 power-law decay is observed in the inertial subrange.

by Kolmogorov turbulence theory over a wide range of wavenumbers, i.e. between 2,000 and 20,000 rad/m where $d\left(\frac{E_{u2}}{\kappa^{-5/3}\varepsilon^{2/3}}\right)/d\kappa$ is equal to 0. The self-similarity of vortical structures in the inertial subrange is then, in the stenotic case, observed throughout the whole systolic time interval under consideration. This suggests that the presence of a narrowed and eccentric orifice, as observed in the stenosed aortic valve under consideration, leads to a flow configuration [14] that sustains the kinetic energy cascade carried by vortical structures. These vortical structures, primarily found near the shear layers between low-velocity regions and the jet [14], shed in a manner similar to what has been studied in homogeneous isotropic turbulence within the inertial range of the spectrum [15,28]. It is worth mentioning that, for the computation of the wavenumber energy spectra, the mode of the log-normal distribution of the correlation function over the points on spherical shells in Fourier space has been taken as the most representative energy level at the considered scalar wavenumber. In the case of the VLth30 bioprosthesis, the power-law with the exponent of −5/3 characteristic of the inertial subrange for the decay of energy does not appear, except at time instants t = 0.1 s, 0.11 s, 0.12 s and 0.245 s, over a narrow range of wavenumbers. Conversely, peaks of energy at κ = 5,000 rad/m and κ = 7,500 rad/m are noticeable as exhibited in Fig. 2 (e). For values of κ ranging from 1,000 to 6,500 rad/m, it has been calculated that the minimum, median and maximum values in time of the $E_u^2/\varepsilon^{2/3}$ curve scale as $\kappa^{-5/3}\ln(\kappa)$, $\kappa^{-5/3}\ln(\kappa)$ and $\kappa^{-7/6}$, respectively. Therefore, in the BioAV case where relatively strong leaflet motions are observed, the decay of kinetic energy does not conform to the energy cascade observed in the inertial subrange for canonical turbulent flows. In the Ulth0 BioAV case, the curve of $d\left(\frac{E_{u2}}{\kappa^{-5/3}\varepsilon^{2/3}}\right)/d\kappa$ equals 0 over wavenumbers ranging from 4,000 to 9,000 rad/m for time instances between t = 0.12 s and t = 0.19 s. Interestingly, these instants correspond to the times at which the KHI at the shear layers establishes itself, as discussed in [14]. This implies that KHI leads to an energy decay that aligns with Kolmogorov's −5/3 power-law prediction over a narrow range of wavenumbers κ. Furthermore, during the instants when KHI is present, high levels of turbulent KE dissipation are observed, as depicted in Fig. 3 (b). In Fig. 2 (f), we observe that, for scalar wavenumbers from 1,000 and 6,000 rad/m, the minimum, median and maximum in time of $\frac{E_{u2}}{\varepsilon^{2/3}}$ scale as κ^{-2}, $\kappa^{-4/3}$ and $\kappa^{-3/2}$, respectively.

Fig. 3 (a) presents the time evolution of the Kolmogorov length scale derived from the dissipation rate of turbulent KE (ε) computed over the spherical shells (cf. Fig. 1). This length scale is the smallest in the stenotic case with a value of about 20 μm constant over systole. In the cases of the two valvular bioprostheses, the Kolmogorov length scale is two to four times the value evaluated downstream of the stenosed aorta. Furthermore, as a consequence of the peak in energy dissipation at t = 0.15 s (Fig. 3 (b)), the Ulth0 case exhibits a reduction in the Kolmogorov length scale, decreasing from 80 to 40 μm. The Kolmogorov length scale in the VLth30 case ranges from 40 to 50 μm over systole. These findings regarding the size of the smallest turbulent eddies, characterised by the Kolmogorov length scale, are in line with the observations made in the first part of the study [14], which analysed the temporal evolution, changes in density and location of coherent vortical structures downstream of the three valve configurations.

The integral length scale $\mathfrak{L}$ is presented in Fig. 3 (c) and was determined by computing the autocorrelation function for each component of the velocity vector **u** in physical space. Subsequently, an equivalent autocorrelation function was calculated over points distributed on spherical surfaces and $\mathfrak{L}$ was obtained by computing the L^2-norm of this equivalent autocorrelation function in each direction. In the stenotic case, the time-averaged integral length scale is approximately 2.8 mm while for the two BioAV prostheses, the time-averaged $\mathfrak{L}$ ranges from 4.5 to 5 mm. The ratio between integral and Kolmogorov length scales is, on average over systole, about 140, 125 and 75 for the stenotic, VLth30 and Ulth0 cases, respectively.

3.2. Energy distribution

In this section, we investigate the distribution of energy intensity in physical space, i.e. over spherical surfaces, as defined in the Methods section. We intend to compare the energy levels among the following cases: the stenosed aorta case, the two newly designed bioprosthetic valves (VLth30 and Ulth0) and a bioprosthetic case presented in the

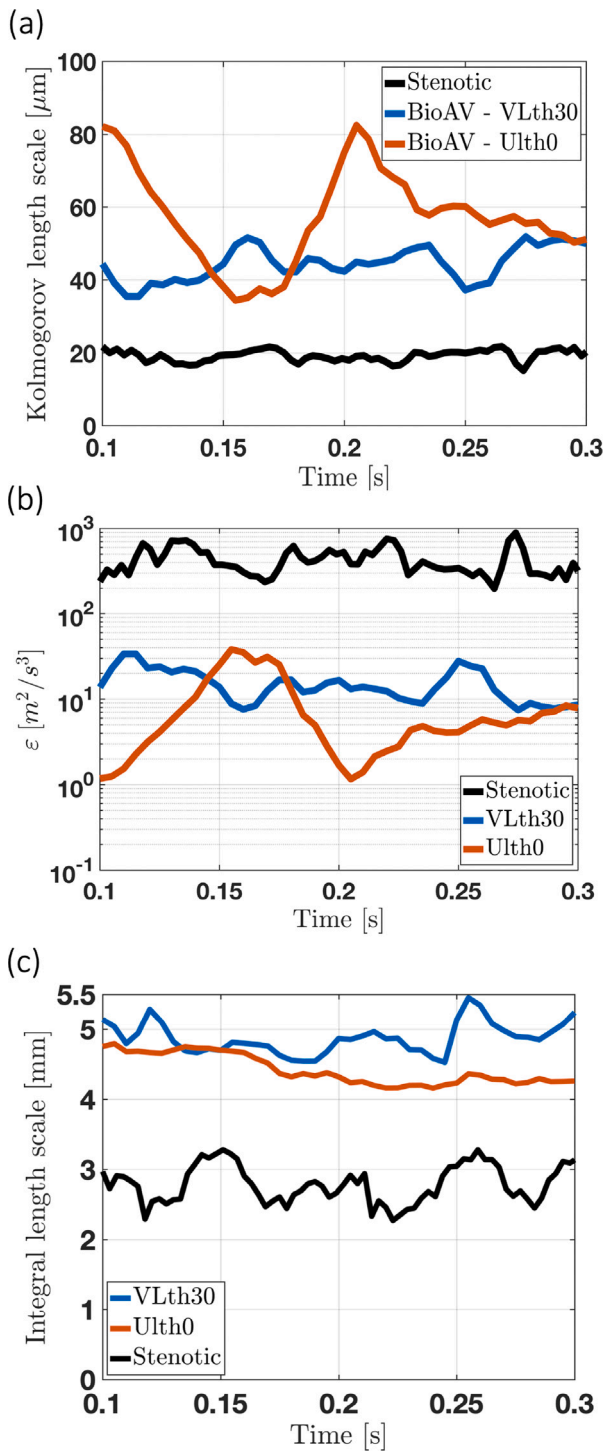

Fig. 3. Time series of turbulence characteristics for the three valvular cases over the systolic phase. (a) Kolmogorov length scale. (b) Dissipation rate of turbulent kinetic energy ε. (c) Integral length scale $\mathfrak{L}$.

study by Gallo et al. [10]. With regard to the turbulent KE intensity, we note in Fig. 4 (a) and (e) that the maximum $\mathbb{I}_{u'^2}$ for the three valvular bioprostheses represents 30% of the maximum $\mathbb{I}_{u'^2}$ in the stenosis case. The time-averaged fluctuating energy intensity for the three BioAV cases is one-sixth that of the stenotic case as illustrated in Fig. 4 (e). We also observe from Fig. 4 (a) that the temporal profile shape for the Ulth0 BioAV case is congruent with the BioAV case investigated in Gallo et al., with the exception that, due to differences in the accelerating and decelerating inflow conditions, the green curve of the BioAV studied by Gallo et al. is shifted in time relative to the Ulth0 curve.

In regards to the fluctuating enstrophy intensity $\mathbb{I}_{\omega'^2}$, the time-averaged value for the VLth30 valvular case is thrice that of the stenotic case and the Ulth0 BioAV case. The elevated levels of fluctuating enstrophy in the VLth30 case arise from the non-axisymmetric and more pronounced leaflet motion, with a displacement magnitude of approximately 2 mm during systole [11,14]. This finding is consistent with the higher levels of streamwise instantaneous and averaged vorticity highlighted in the first part of the study [14]. For the VLth30 case, the times at which a local minimum in the fluctuating enstrophy temporal evolution is found (i.e. t = 0.12, 0.156, 0.21, 0.256 s) correspond to the times at which the area at the vena contracta is maximum [14].

Helicity is the integral over a volume of interest of the inner product between velocity and vorticity vectors. This is closely related to the notion of vortex stretching. In fact, helicity plays an important role in the generation and evolution of vortices. It also tightly connects to the knottedness and the twisting of vortex lines [29,30]. In addition, helicity is known to inhibit the transfer of energy towards smaller scales, since the statistical alignment of velocity and vorticity leads to partial suppression of the non-linear term and to a relatively low dissipation [10]. The results in Fig. 4 (c, d, e) are aligned with this statement. For both the VLth30 and Ulth0 cases, the time-averaged and maximum values of unsigned helicity intensity (III and IV) are 2 to 2.5 times as large as those observed in the stenotic case. Moreover, the curves of signed helicity intensity (Fig. 4 (d)) for the VLth30 and Ulth0 BioAVs exhibit peaks with a magnitude 10 times larger than those observed in the stenotic case and in the BioAV case investigated in Gallo et al.. The differences in signed helicity intensity compared to the results by Gallo et al. may stem from several factors. First, the spatial integration performed over the entire fluid volume, encompassing the straight ascending aorta and the three sinuses, in Gallo et al.'s study differs from the integration over spherical surfaces near the valve orifice in the present study. The phase-averaging over 20 cardiac cycles conducted by Gallo et al. also represents a difference in the computation of fluctuating and averaged field quantities, such as helicity. Lastly, the leaflet dynamics in Gallo et al. are modelled using a simplified mass–spring system, potentially leading to discrepancies in leaflet motion. These discrepancies can indeed impact flow features and downstream helicity. Furthermore, as emphasised in the previous section, the exponent of the power law governing the three-dimensional wavenumber spectra (represented by the median, maximum, and minimum curves over time) for the two BioAV cases is greater than the −5/3 value predicted by Kolmogorov for isotropic and homogeneous turbulence, a value which has been observed to hold in the stenotic case. This suggests an inhibition of non-linear advection in the energy cascade, likely due to the presence of local helical flow motion, in the region near the bioprosthetic valvular orifice. Finally, it is worth noting in Fig. 4 (d) that the signed helicity intensity $\mathbb{I}_{h'^2}$ in the VLth30 case exhibits an average negative value across spherical shells between t = 0.1 and t = 0.15 s. This indicates the prevalence of counter-clockwise helical structures in the vicinity of the valvular orifice during this time period. In fact, as depicted in Fig. S1 in the SI and in the corresponding videos, leaflet motion advects the helical structures throughout the whole ascending aorta. The helical structures close to the jet border are colour-coded in red, indicating a clockwise swirling motion, while those near the aortic wall are colour-coded in blue, showing counter-clockwise helical motion throughout systole. Conversely, in the Ulth0 BioAV case, the signed helicity intensity remains positive until t = 0.2 s, suggesting the dominance of clockwise helical motion. After t = 0.15 s, a decrease in $\mathbb{I}_{h'^2}$ is observed, eventually reaching small negative values until t = 0.28 s. This trend can also be observed from the Fig. S1 in the SI and in the corresponding videos where the number of helical structures is lower in this case, with a peak throughout systole when KHI arises (i.e. between t = 0.12 and 0.21 s). During this time interval, the helical structures alternate between blue and red but the intensity

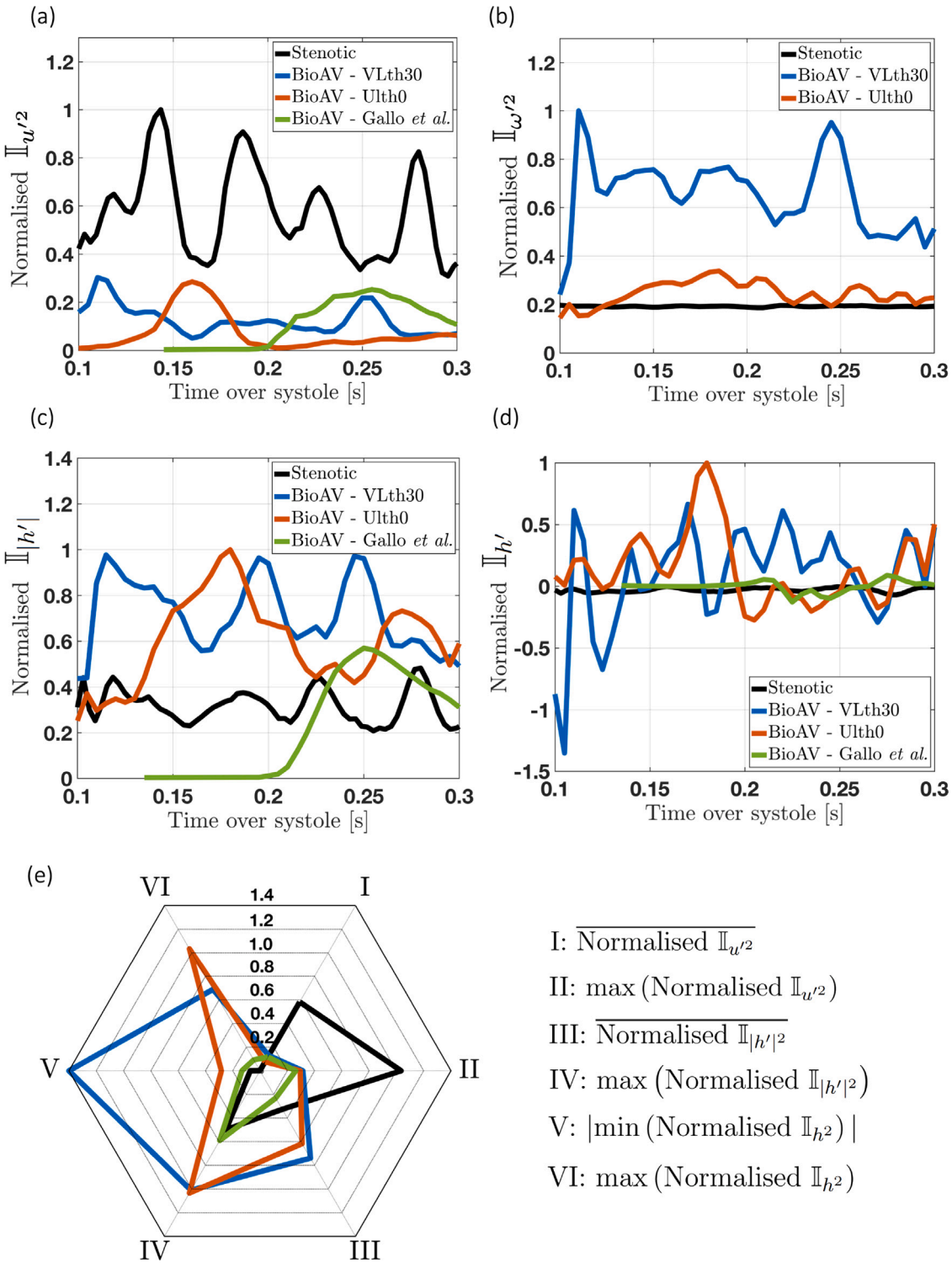

Fig. 4. Time series over systole of normalised (a) intensity of fluctuating KE, (b) intensity of fluctuating enstrophy, (c) intensity of unsigned fluctuating helicity and (d) intensity of signed fluctuating helicity. The three valvular cases investigated in this study are plotted along with the valvular case presented in Gallo et al. [10]. (e) Spider chart of the time-averaged ($\overline{\circ}$) and maximum normalised $\mathbb{I}_{u'^2}$ (I and II) and $\mathbb{I}_{|h'|^2}$ (III and IV). The maximum and absolute minimum values of normalised $\mathbb{I}_{h'^2}$ is also displayed (V and VI).

of signed fluctuating helicity remains positive between $t = 0.1$ and 0.2 s and drops thereafter. Worthy of note is that the intensity of signed fluctuating helicity is zero on average over spherical shells in the severe stenotic case (see Fig. 4 (d)), facilitating the non-linear energy transfer in the inertial range of the wavenumber spectra, as highlighted in the previous sub-section.

3.3. Anisotropy in the modal kinetic energy and helicity intensity

In this section, the novel quantities defined in Eqs. (27) and (28) representing the modal KE anisotropy $\mathbb{I}_{p_s}^{\text{flow anis}}$ and normalised helicity intensity $\mathbb{I}_{p_s}^{h|_{\text{sph}}}$, respectively, are characterised and correlated through probability density function (PDF) and spatial heatmaps, unrolled by

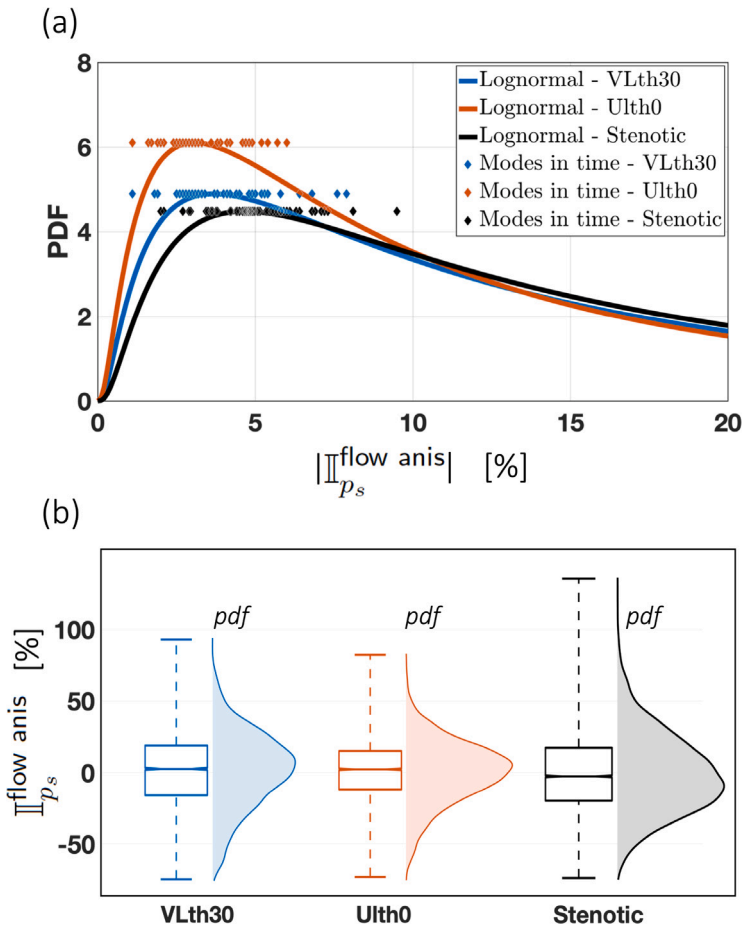

Fig. 5. Probability distributions of the modal KE anisotropy intensity. (a) Fitted log-normal probability density function (PDF) for the three valve configurations, the mode of the PDFs was used in the spectral analysis part of the study. The rhombi represent the modes of the log-normal distribution fitted for each instant considered over peak systole. (b) Boxplots and distribution for the comparison of the shape of the distributions for the three valvular cases.

means of a cylindrical projection from the distribution over spherical shells described in the Methods section.

In Fig. 5 (a), the log-normal PDF fitted to the absolute value of $\mathbb{I}^{\text{flow anis}}_{p_s}$ distributed over the spherical surfaces (cf. Fig. 1) and evolving in time is presented. We observe that, across all time instances considered between $t = 0.1$ and 0.3 s, the mode of the log-normal distribution for $|\mathbb{I}^{\text{flow anis}}_{p_s}|$ in the stenotic case is 35% and 65% higher than the modes of the log-normal distributions in the VLth30 and Ulth0 cases, respectively. In the same figure, the modes for each considered time instance are represented with diamond markers. The stenotic case displays a maximum mode value of 9.5%, compared to 7.9% for the VLth30 case and 6% for the Ulth0 case. We can also notice this trend in the PDFs and boxplots of $\mathbb{I}^{\text{flow anis}}_{p_s}$ shown in Fig. 5 (b) for the three valvular cases. In fact, the maximum values of $\mathbb{I}^{\text{flow anis}}_{p_s}$ equals 136%, 92% and 81.3% for the stenotic, VLth30 and Ulth0 cases, respectively. In Fig. 5 (b), it can be seen that the median value for $\mathbb{I}^{\text{flow anis}}_{p_s}$ is positive for the two bioprosthesis cases, with a value of around 1.5% whereas the median value for the stenotic is negative and equal to −2.2%. The asymmetry in the probability distribution of modal KE is indicative of asymmetries in jet flows, which are associated with complex vortex dynamics [14], especially when helicity is non-zero [28]. The skewness of the VLth30 probability density function (PDF) is negative, while that of the stenotic PDF is positive. Both cases exhibit a similar interquartile range (IQR) value of 35%. In contrast, the PDF for the Ulth0 case appears almost symmetric, as emphasised by Corso et al. [14], as a consequence of a triangular jet flow topology with low eccentricity distance throughout systole. As a result of this more symmetric flow topology, the IQR in the Ulth0 case equals 27%, which is 23% smaller than that for the other two valve cases.

In Fig. 6, the spatial distribution of the absolute value of the modal KE anisotropy intensity $|\mathbb{I}^{\text{flow anis}}_{p_s}|$ (Eq. (27)) is presented by unrolling the sphere through a cylindrical projection. The standard deviation σ over the investigated time instances and the time average ($\overline{\circ}$) of $|\mathbb{I}^{\text{flow anis}}_{p_s}|$ are compared based on the two-dimensional (α, φ) maps. In the stenotic case, in Fig. 6 (c), we observe that $|\overline{\mathbb{I}^{\text{flow anis}}_{p_s}}|$ reaches its maximum, with values ranging from 25% to 40%, at the azimuthal angles corresponding to the locations of commissures 1, 2, and 3 (i.e., at $\alpha \approx -120°$, $-10°$ and $80°$). The standard deviation $\sigma\left(|\mathbb{I}^{\text{flow anis}}_{p_s}|\right)$ attains peak values of 15% in the region between commissures 1 and 3. This region corresponds to a zone where low flow velocities and few coherent vortical structures with limited stretching are found [14]. We also notice a region with moderately high values of 5% for $\sigma\left(|\mathbb{I}^{\text{flow anis}}_{p_s}|\right)$ at elevation angles $\varphi > 50°$. Concerning the VLth30 BioAV, Fig. 6 (e) and (f) reveal that $\sigma\left(|\mathbb{I}^{\text{flow anis}}_{p_s}|\right)$ and $|\overline{\mathbb{I}^{\text{flow anis}}_{p_s}}|$ are the largest for $\varphi < -50°$. In addition, peak values in the standard deviation of absolute value of modal KE anisotropy, reaching 15%, are found at azimuthal angles of $-150°$, $-30°$ and $90°$. We observe that these peaks are aligned with the position of the three posts of the BioAV ring (see Fig. 2 of the first part of the study for the description of the BioAV geometries [14]). With respect to the Ulth0 bioprosthesis, the values for the spatial distribution of $\sigma\left(|\mathbb{I}^{\text{flow anis}}_{p_s}|\right)$ and $|\overline{\mathbb{I}^{\text{flow anis}}_{p_s}}|$ are noticeably lower, as previously indicated based on the PDFs and the modes of the fitted log-normal distribution. However, peaks in the time-averaged absolute value of modal KE anisotropy $|\overline{\mathbb{I}^{\text{flow anis}}_{p_s}}|$ can be observed in Fig. 6 (i). Similar to the VLth30 case, these peaks align with the positions of the valvular ring posts. This sheds light on how the presence of

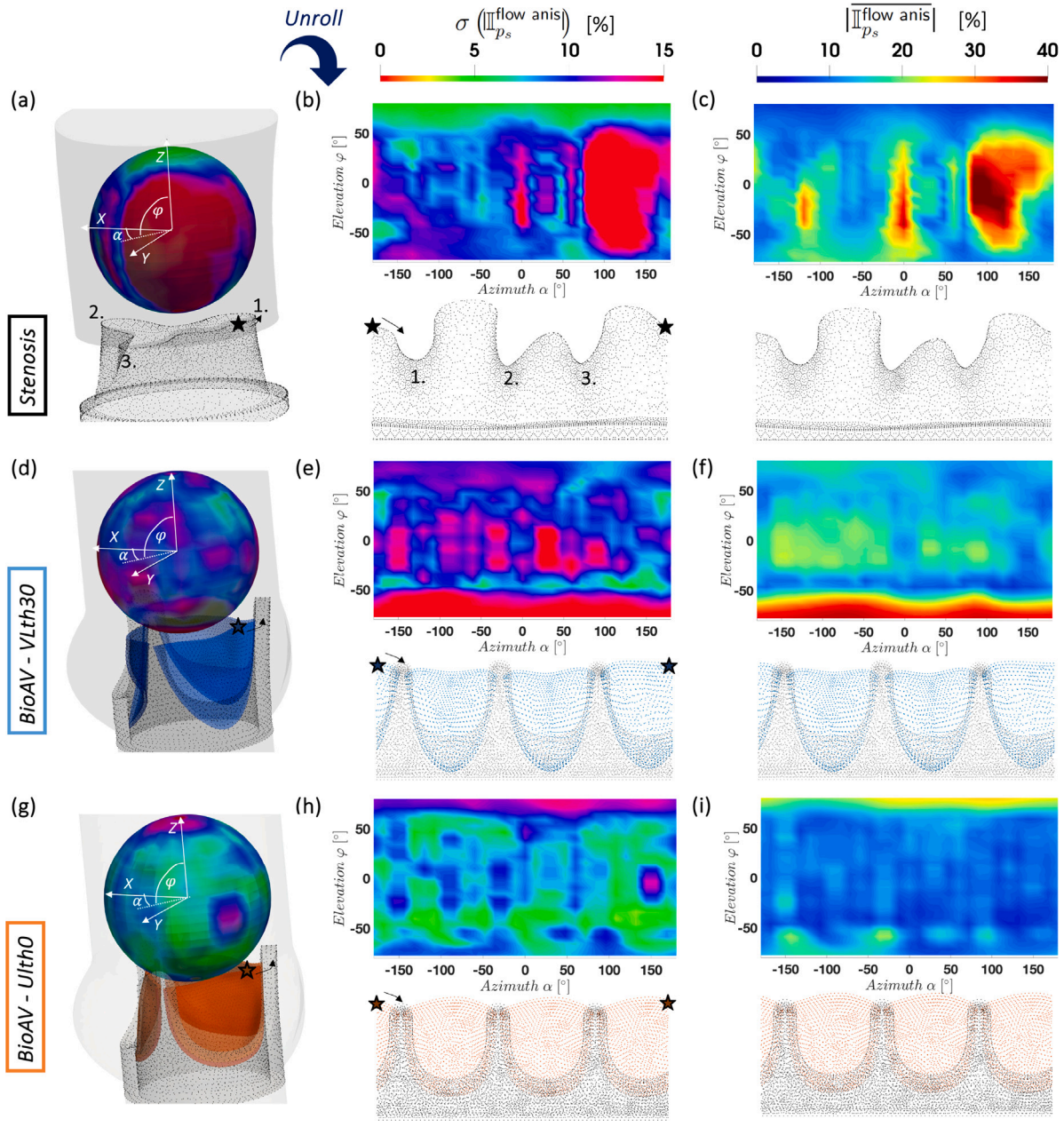

Fig. 6. Spatial distribution and statistical description, including the standard deviation σ and the temporal average value of the time-dependent modal KE anisotropy fields $|\mathbb{I}_{p_s}^{\text{flow anis}}|$ obtained on spherical shells near the valvular orifice. The geometries of the spheres and orifice are projected onto a rectangular map using a cylindrical map projection, also known as the Mercator projection. In this map, the azimuthal angle α is represented on the x-axis and the elevation angle φ is represented on the y-axis. The stenotic case is presented in (a, b, c), the valvular case with the design VLth30 in (d, e, f) and the case of the BioAV with the design Ulth0 in (g, h, i).

a robust supporting ring geometry influences the generation of flow disturbances, disrupting flow symmetry.

Fig. 7 presents the comparison and point-to-point correlation between the unrolled maps of time-averaged modal KE anisotropy and normalised helicity intensity. The interest in conducting such a correlation lies in the findings presented by Gallo et al. [10], which reveal a strong linear relationship between phase-averaged and fluctuating helicity and KE. In the study by Gallo et al., the correlation was established based on volume-averaged energy and helicity over the cardiac cycle. In Fig. 7 (b, f, j), the heatmaps of time-averaged normalised helicity intensity are displayed. These maps suggest that the spatial distribution of $\overline{\mathbb{I}_{p_s}^{h|\text{sph}}}$ is inversely proportional to the spatial distribution of $\overline{|\mathbb{I}_{p_s}^{\text{flow anis}}|}$, as depicted in the maps shown in Fig. 7 (a, e, i). In order to conduct a point-to-point correlation for the three valvular cases, a non-linear least-square regression problem is solved. To achieve this, the points on the (α, φ) maps are divided into two sets: one is the training set used for fitting the coefficients A and B in the power-law equation of the form $\overline{|\mathbb{I}_{p_s}^{\text{flow anis}}|} = A\left[\overline{\mathbb{I}_{p_s}^{h|\text{sph}}}\right]^B$ and the other is the testing set used to evaluate the prediction accuracy. The latter is assessed through the coefficient of determination (R^2) [3,11,13]. From Fig. 7 (c, g, k), it can be noted that, for the three valve configurations, $|\mathbb{I}_{p_s}^{\text{flow anis}}|$ inversely correlates with $\overline{\mathbb{I}_{p_s}^{h|\text{sph}}}$ as demonstrated by the negative fitted exponent B (cf. Table 1 in the supporting information). The accuracy of the regression from R^2 evaluated on the training (Fig. 7 (g)) and testing (Fig. 7 (h)) data points of the heatmaps is the highest with a value of about 0.75 in the VLth30 BioAV case. This valve design leads to non-axisymmetric leaflet motions in relation the centreline with displacement magnitude of about 2 mm during systole (see Fig. S1 of the SI of [14]). The eccentricity of the jet calculated in a proximal

cross-section as well as the area at the vena contracta is also evaluated in [14] and it has been shown that the leaflet motions produce stronger levels of vortex stretching magnitude as compared to the Ulth0 BioAV case, whose leaflets are almost immobile throughout systole. The latter case exhibits a low R^2 of 0.1 based on both the training and testing data points from the heatmaps or spherical shells, indicating a weaker anti-correlation between modal KE anisotropy and normalised helicity intensity. Regarding the stenotic case, the correlation accuracy on the training dataset is moderate with $R^2 = 0.43$ (Fig. 7 (c)) while the coefficient of determination drops to 0.1 on the testing data points (Fig. 7 (d)). The variation in the prediction accuracy and strength of correlation among the three valvular cases under examination is an interesting point to analyse. In fact, as stated by Gallo et al. [10], the role of helicity in the generation and evolution of turbulence may depend on the topology of the flow and vortices, namely dependent on the vortex stretching and tilting process. In the first part of this study [14], we highlight three different jet flow configurations connected to the valvular orifice architecture. It can then be postulated that flow asymmetries introduced by moving leaflets, as highlighted in the VLth30 case by the presence of a jet with high velocities in a proximal cross-section [14], which changes shape over time and exhibits varying eccentricity, result in higher levels of KE anisotropy close to the orifice and a stronger inverse correlation with normalised helicity intensity. Finally, for both BioAV cases, similarly to what was observed for $\overline{|\mathbb{I}_{p_s}^{\text{flow anis}}|}$ and $\sigma\left(|\mathbb{I}_{p_s}^{\text{flow anis}}|\right)$, high values of $\overline{\mathbb{I}_{p_s}^{h|\text{sph}}}$ are found at azimuthal angles where the three valve ring posts (indicated by the letter P in Fig. 7) are located.

3.4. Leaflet dynamics analysis and anisotropy in the valve motion

Since we previously highlighted the potential impact of moving leaflets on the degree of correlation between KE anisotropy intensity and normalised helicity intensity, in Fig. 8 (a, b, e, f), we closely examine the KE carried by the moving structural components of the two BioAVs.

As demonstrated in Fig. 8 (a) and (b), the standard deviation of leaflet displacement magnitude over time in the VLth30 case is four times that in the Ulth0 case, as highlighted in the first part of the study [14]. The standard deviation of the displacement magnitude in the supporting ring of the two BioAVs is highest at the extremity of the three posts. In the first part [14], hairpin-like vortices were observed near the three posts as a consequence of the motion of the leaflets and posts, particularly when the gap between the leaflets and the ring post widens. In Fig. 8 (b), the spatial distribution of the standard deviation of biomechanical KE anisotropy for the VLth30 case shows strong variation amongst the three leaflets while for the Ulth0 BioAV, $\sigma\left(\mathbb{I}_{p_s}^{\text{flow anis}}\right)_{\text{norm}}$ is more uniformly distributed. With a view to establishing a correlation between the flow and structural anisotropy intensity, we have plotted the graphs depicting the standard deviation of flow modal KE anisotropy and biomechanical KE anisotropy. These values are averaged over the elevation angles φ and normalised to range from 0 to 1, as shown in Fig. 8 (c) and (g). The cross-correlation function of the curves in the graphs of Fig. 8 (c) and (g) has been calculated and is presented in Fig. 8 (d) and (h). In the case of the VLth30 BioAV, the graph indicates a strong correlation between flow and biomechanical anisotropy, as the cross-correlation function reaches its peak at an azimuthal shift of 0°. In the case of the Ulth0 BioAV, the cross-correlation function in Fig. 8 (h) indicates a relatively strong correlation, with peak values occurring at azimuthal shifts ranging from −10° to 0°. However, the curves in Fig. 8 (g) suggest an inverse correlation, as the minima in $\sigma\left(\mathbb{I}_{p_s}^{\text{flow anis}}\right)_{\text{norm}}$ align with the maxima in $\sigma\left(\mathbb{I}_{p_m}^{\text{struct anis}}\right)_{\text{norm}}$. This suggests that, following a train of thought relying on transitivity, motions within the structural components of the VLth30 BioAV leave an imprint on the downstream flow KE, which, in turn, exhibits a close correlation with vorticity intensity and vortex stretching [14] and with the levels of helicity intensity. It has also been hypothesised that helicity plays a role in influencing the modal KE spectrum, particularly within the inertial sub-range, which, in the VLth30 case, deviates from the typical energy decay observed in canonical turbulent flows.

4. Conclusions

The findings for each valvular case regarding this second part of the study can be summarised as follows:

- Stenotic case: The decay of energy, observed across different time instances, reflects fluctuations in flow behaviour. It adheres to Kolmogorov's −5/3 power-law over a broad range of scalar wavenumbers, indicating the presence of a cascade of kinetic energy typical of canonical turbulence. The Kolmogorov length scale is smallest in the stenotic case, signifying the presence of smaller turbulent eddies. Moreover, the maximum TKE in the stenotic case surpasses that of the BioAV cases by threefold, with the time-averaged fluctuating energy intensity being six times higher in the stenotic case compared to the two BioAV cases. Moreover, the mode of the log-normal distribution for the flow modal KE anisotropy, $\mathbb{I}_{p_s}^{\text{flow anis}}$, is larger that of the VLth30 case by 35% and the Ulth0 case by 65%. While the median value of the distribution of $\mathbb{I}_{p_s}^{\text{flow anis}}$ is negative (−2.2%) in the stenotic case, it is positive for the bioprostheses. Additionally, the spatial distribution of $\overline{|\mathbb{I}_{p_s}^{\text{flow anis}}|}$ peaks at azimuthal angles corresponding to immobile leaflet commissures' position, with the highest standard deviation observed between commissures 1 and 3.
- VLth30 BioAV case: The energy decay over time from the spectral analysis exhibits smaller variations compared to the stenotic case and deviates from Kolmogorov's −5/3 power-law, instead showing peaks of energy at specific wavenumbers. Larger eddies are noted as evidenced by the integral and Kolmogorov length scales being twice as large compared to the stenotic case. Moreover, the time-averaged fluctuating enstrophy intensity is notably higher in the VLth30 case, reaching three times that of both the stenotic and Ulth0 cases. This increase is attributed to the non-axisymmetric motion of the leaflets, which generates higher levels of vorticity. Interestingly, the local minima in enstrophy coincide with times of maximum area at the vena contracta, suggesting a relationship between leaflet motion and flow characteristics. In terms of modal KE anisotropy, the VLth30 case exhibits a spatial distribution that peaks at azimuthal angles aligned with the valve ring posts, with the highest standard deviation observed near these posts. This spatial distribution contrasts with the more uniform distribution observed in the Ulth0 BioAV case. Furthermore, there is a strong inverse correlation between modal KE anisotropy and normalised helicity intensity in the VLth30 case, with a larger coefficient of determination R^2 compared to the stenotic and Ulth0 BioAV cases. Examining the KE carried by the valve structural elements, the VLth30 BioAV displays a significantly higher standard deviation of leaflet displacement magnitude over time compared to the Ulth0 BioAV case, with the highest standard deviation observed in the supporting ring at the extremity of the three posts. A strong correlation between the standard deviation of flow and biomechanical anisotropy, $\sigma\left(|\mathbb{I}_{p_s}^{\text{flow anis}}|\right)$ and $\sigma\left(|\mathbb{I}_{p_m}^{\text{struct anis}}|\right)$, averaged over the elevation angle is observed. The VLth30 BioAV case demonstrates a complex interplay between valve design, leaflet motion and energy-based flow features, with asymmetric leaflet motions influencing downstream flow KE distribution and anisotropy as well as normalised helicity intensity $\overline{\mathbb{I}_{p_s}^{h|\text{sph}}}$.
- Ulth0 BioAV case: The variations in the energy spectra trend over time are limited due to the stable motion of the leaflets. The decay of energy aligns with Kolmogorov's −5/3 power-law within the inertial sub-range only at specific time instances characterised

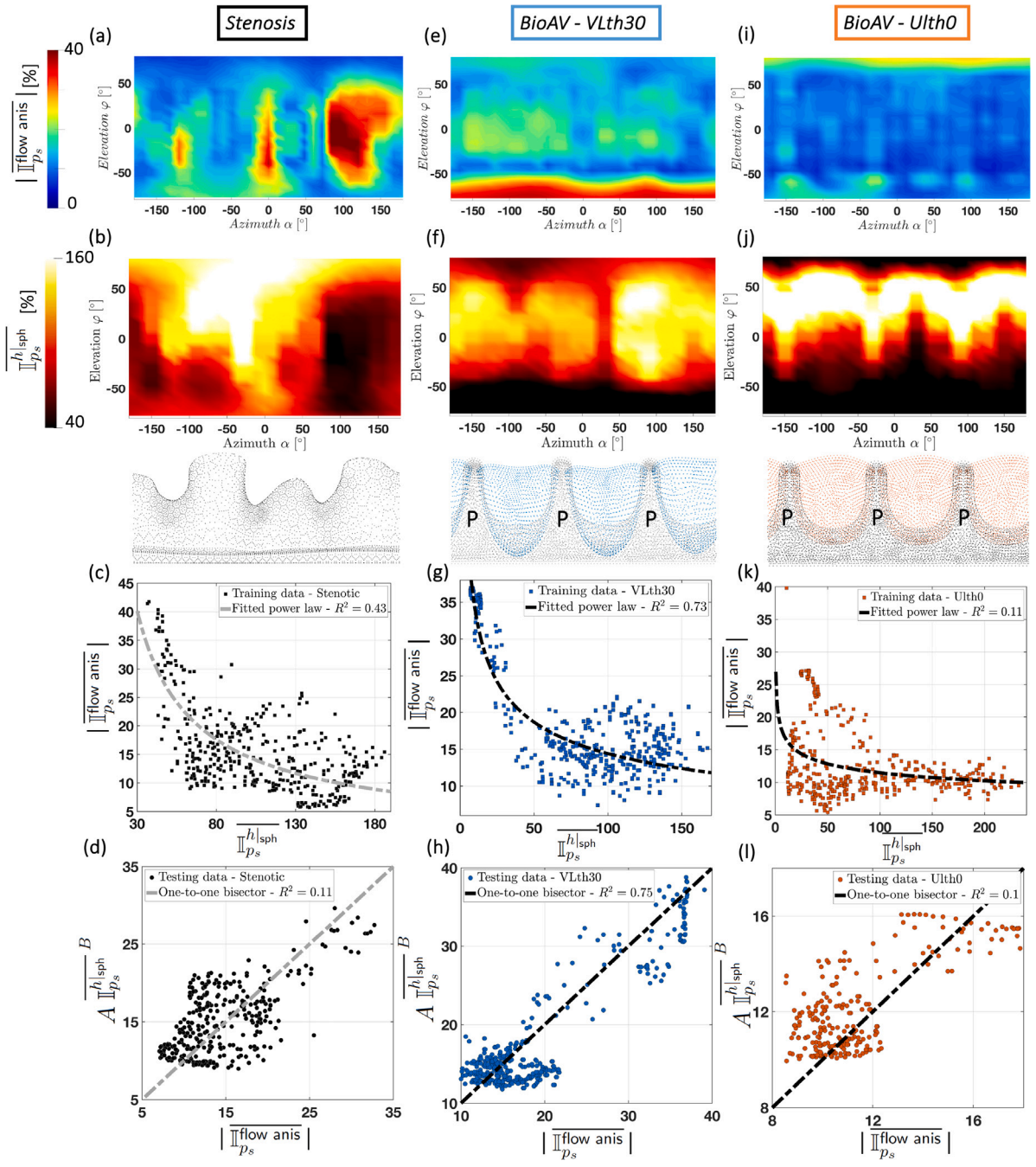

Fig. 7. Anti-correlation between $|\overline{\mathbb{I}^{\text{flow anis}}_{p_s}}|$ and $\overline{\mathbb{I}^{h|_{\text{sph}}}_{p_s}}$ over spherical shells close to the valvular orifice (cf. Fig. 1). The colour-coded distribution map of the temporal average of $|\mathbb{I}^{\text{flow anis}}_{p_s}|$ for the three valvular configurations under consideration is displayed in (a, e, i). The distribution heat map of time-averaged normalised helicity intensity $\mathbb{I}^{h|_{\text{sph}}}_{p_s}$ is displayed in (b, f, j) for the three valvular cases. (c, g, k) Scatter plots of $|\overline{\mathbb{I}^{\text{flow anis}}_{p_s}}|$ as a function of $\mathbb{I}^{h|_{\text{sph}}}_{p_s}$. The two coefficients A and B of a power law correlating the two quantities are fitted through the resolution of a non-linear least-square minimisation problem [3,11,13]. The accuracy of the training prediction is evaluated using the coefficient of determination R^2. The accuracy of the prediction based on the testing dataset points for the three valvular cases is presented in (d, h, l).

by the presence of Kelvin–Helmholtz instability. The size of the eddies in this scenario is estimated to be twice to thrice as large as those calculated in both the stenotic and VLth30 BioAV cases. Regarding the helicity intensity, both the time-averaged and maximum values of unsigned fluctuating helicity intensity are notably larger, ranging from 2 to 2.5 times, compared to the stenotic case. Similarly, the signed helicity intensity exhibits peaks that are 10 times larger than those observed in the stenotic case. The temporal evolution of signed helicity intensity and helical structures indicates the dominance of clockwise helical motion until $t = 0.2$ s, followed by a subsequent decrease in fluctuating helicity intensity. It is speculated that the higher levels of fluctuating helicity intensity inhibits energy transfer towards smaller scales. In terms of modal flow KE anisotropy $\mathbb{I}^{\text{flow anis}}_{p_s}$, both the mode and median values of the distribution are lower than those observed in the stenosed case. The spatial distribution of $\sigma\left(|\mathbb{I}^{\text{flow anis}}_{p_s}|\right)$ is more uniform and exhibits lower values compared to both the VLth30 BioAV and stenotic cases. Interestingly, the spatial distribution of time-averaged flow KE anisotropy and normalised helicity intensity peaks at azimuthal angles aligned with the valve ring posts. Indeed, a relatively strong inverse correlation

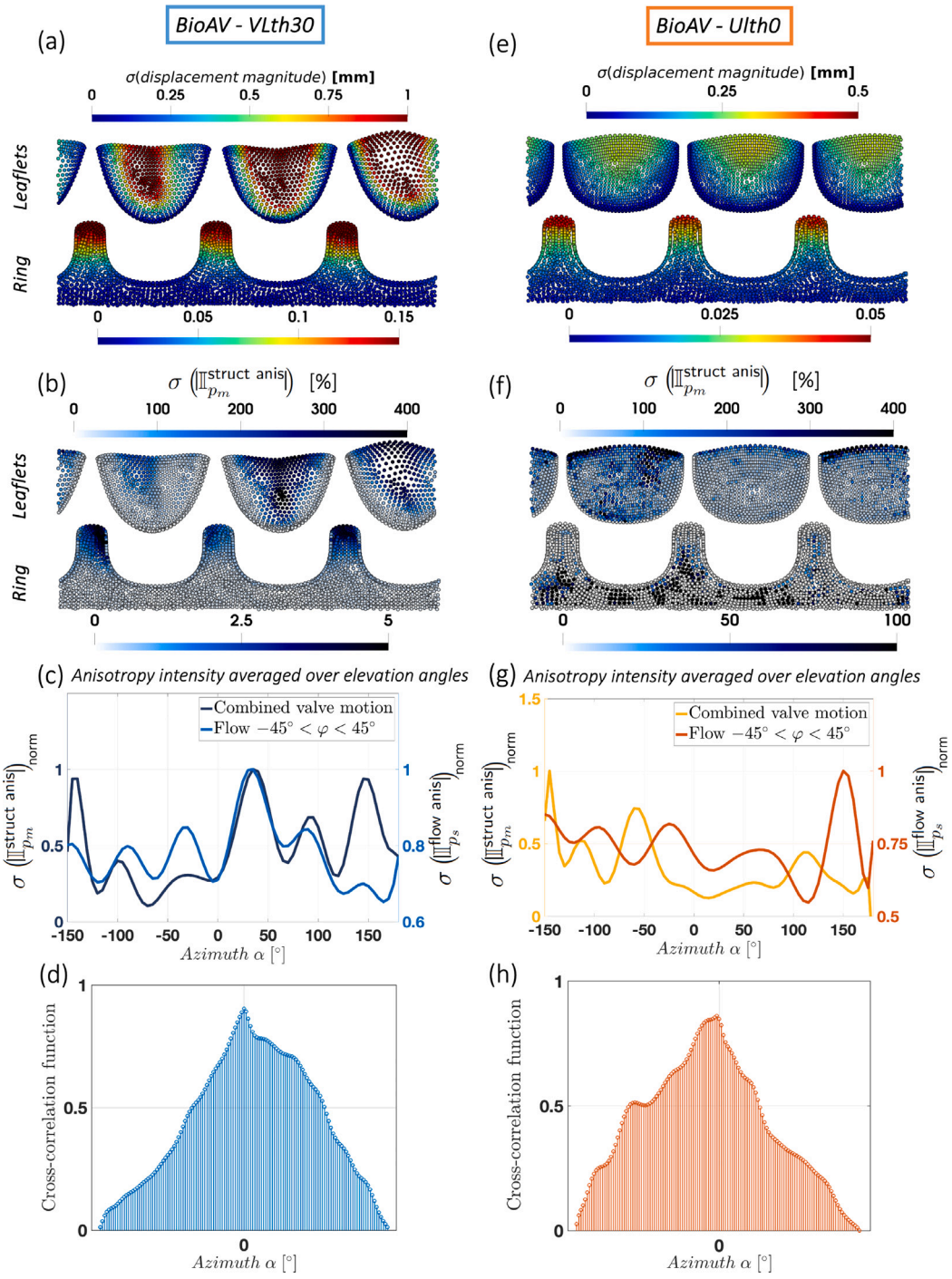

Fig. 8. Comparison and correlation between the anisotropy in the leaflet and ring motion of the two bioprosthetic valves (VLth30 and Ulth0) and anisotropy of the modal kinetic energy in the flow in the vicinity of the valve orifice. (a, e) Standard deviation σ of the unrolled point distribution of the anisotropy intensity based upon the valve kinetic energy. (b, f) Standard deviation σ of the time-dependent unrolled spatial distribution of the displacement magnitude in the two valves. (c, g) Comparison of the standard deviation of the anisotropy intensity in the valve motion and in the flow averaged over the elevation angle φ as a function of the angle α. (g, h) Cross-correlation functions between the two $\sigma\left(\mathbb{I}^{\text{flow anis}}_{p_s}\right)_{\text{norm}}$ and $\sigma\left(\mathbb{I}^{\text{struct anis}}_{p_m}\right)_{\text{norm}}$ curves as a function of α.

is observed between the standard deviation of flow and biomechanical anisotropy when averaged over elevation angles. This suggests a more prominent influence of the presence of the valve ring posts on flow energy levels, particularly in the absence of important leaflet motions.

The present study highlights the influence of valve architecture on turbulence characteristics in the ascending aorta near the valvular orifice. The complex interplay among flow configuration, helicity, leaflet motion and kinetic energy anisotropy is discussed and the investigation of flow disturbances associated with turbulence relies on advanced energy-based analyses. These analyses include a dedicated three-dimensional spectral analysis and the introduction of new quantities, namely the modal and biomechanical kinetic energy anisotropy. The presented results and discussion are in line with the conclusions drawn from the first part of the study [14], indicating the improved performance of the Ulth0 BioAV design. This improvement is evidenced by a reduction in fluctuating kinetic energy, modal KE anisotropy

and larger turbulent length scales, as well as an increase in positive signed fluctuating helicity intensity inhibiting kinetic energy transfer towards smaller eddy sizes. Further enhancements to this valve design could involve controlling the generation of KHI by adjusting leaflet material properties to slightly reduce their rigidity. Moreover, considering the energy-based correlation between haemodynamics and valve biomechanics, reductions in modal KE anisotropy levels could be achieved through modifications to the design of the supporting ring of the leaflets. The limitations of the present second part of the two-part study include the assumption of rigid calcified leaflets due to extensive calcification in the stenotic numerical model and the limited time span simulated, covering only the systolic phase of one cardiac cycle. In addition, in line with the objective of studying haemodynamics solely originating from the valvular orifice and its correlation with leaflet dynamics, kinetic energy, helicity and enstrophy have not been investigated within the three sinuses. Nevertheless, with the aim of restoring a more physiological flow in the aorta, synonymous with examining and enhancing jet flow stability connected to valve architecture, the proposed advanced analyses provide valuable insights into the haemodynamic performance of valve prostheses. This is achieved through the assessment of energy distribution and anisotropy near the orifice, complemented by the findings of the first part of the study.

The detailed two-part computational study lays the foundation for a comprehensive set of analyses, forming a robust platform for evaluating the performance of valve prostheses. This platform aims to facilitate the development and fine-tuning of enhanced and personalised valve designs, with the goal of mitigating the adverse consequences associated with aortic valve replacement.

CRediT authorship contribution statement

Pascal Corso: Writing – review & editing, Writing – original draft, Visualization, Validation, Software, Resources, Project administration, Methodology, Investigation, Formal analysis, Data curation, Conceptualization. **Dominik Obrist:** Resources, Funding acquisition.

Declaration of competing interest

The authors declare that they have no known competing financial interests or personal relationships that could have appeared to influence the work reported in this paper.

Data availability

All data and materials needed to evaluate the conclusions of this paper are present in the main text or supplementary materials. Processable data files can be obtained from the first author.

Acknowledgements

This work was supported by the computing resources from the Swiss National Supercomputing Centre (CSCS) under project IDs s1012, s1153 and s1210.

P. Corso would like to thank F. B. Coulter (ETH Zürich) for providing the computer-aided sketch of the sheet-like leaflet geometry. This sketch was instrumental in generating the final three-dimensional and volumetric geometrical model of the VLth30 BioAV for the present study. P. Corso also acknowledges the support of M. G. C. Nestola, a researcher at Università della Svizzera italiana (USI), for the provided information on the solid solver and on the part of the code dealing with the coupling of the two solvers.

Appendix A. Supplementary data

Supplementary material related to this article can be found online at https://doi.org/10.1016/j.compbiomed.2024.108552.

References

[1] B.R. Lindman, M.-A. Clavel, P. Mathieu, B. Lung, P. Lancellotti, C.M. Otto, Ph Pibarot, Calcific aortic stenosis, Nat Rev Dis Primers 2 (2016).
[2] P. Corso, U. Gülan, N. Cohrs, et al., Comprehensive in vitro study of the flow past two transcatheter aortic valves: Comparison with a severe stenotic case, Ann. Biomed. Eng. 47 (11) (2019) 2241–2257.
[3] P. Corso, G. Giannakopoulos, U. Gulan, et al., A novel estimation approach of pressure gradient and haemodynamic stresses as indicators of pathological aortic flow using subvoxel modelling, IEEE Trans. Biomed. Eng. 68 (3) (2021) 980–991.
[4] A.J. Yoganathan, S. He, S.C. Jones, Fluid mechanics of heart valves, Annu. Rev. Biomed. Eng. 6 (2004) 331–362.
[5] J.S. Aluru, A. Barsouk, K. Saginala, P. Rawla, A. Barsouk, Valvular heart disease epidemiology, Med. Sci. 10 (2) (2022).
[6] V. Nguyen, M. Michel, H. Eltchaninoff, et al., Implementation of transcatheter aortic valve replacement in France, J. Am. Coll. Card. 71 (15) (2018).
[7] H. Baumgartner, V. Falk, J.J. Bax, M. De Bonis, et al., ESC/EACTS guidelines for the management of valvular heart disease, Eur. Heart J. 38 (36) (2017) 2739–2791.
[8] S. Bailoor, J.-H. Seo, L. Dasi, et al., A computational study of the hemodynamics of bioprosthetic aortic valves with reduced leaflet motion, J. Biomech. 120 (2021).
[9] B. Becsek, L. Pietrasanta, D. Obrist, Turbulent systolic flow downstream of a bioprosthetic aortic valve: Velocity spectra, wall shear stresses, and turbulent dissipation rates, Front. physiol. 11 (2020) 539–575.
[10] D. Gallo, U. Morbiducci, M.D. de Tullio, On the unexplored relationship between kinetic energy and helicity in prosthetic heart valves hemodynamic, Internat. J. Engrg. Sci. 117 (2022).
[11] E. Tsolaki, P. Corso, R. Zboray, J. Avaro, et al., Multiscale multimodal characterization and simulation of structural alterations in failed bioprosthetic heart valves, Acta Biomater. 169 (10) (2023) 138–154.
[12] F. Sotiropoulos, T.B. Le, A. Gilmanov, Fluid mechanics of heart valves and their replacements, Annu. Rev. Fluid Mech. 48 (2016) 259–283.
[13] P. Corso, J. Walheim, H. Dillinger, et al., Toward an accurate estimation of wall shear stress from 4D flow magnetic resonance downstream of a severe stenosis, Magn. Res. Med. 86 (3) (2021) 1531–1543.
[14] P. Corso, D. Obrist, On the role of aortic valve architecture for physiological hemodynamics and valve replacement, Part I: flow configuration and vortex dynamics, Comput. Biol. Med. (2024).
[15] S.B. Pope, The scales of turbulent motion, in: Turbulent Flows, Cambridge University Press, 2000, pp. 182–263.
[16] NEK5000 v19.0. Argonne national laboratory, illinois, 2020, [Online]. Available: https://nek5000.mcs.anl.gov.
[17] F.B. Coulter, M. Schaffner, J.A. Faber, A. Rafsanjani, R. Smith, H. Appa, P. Zilla, D. Bezuidenhout, A.R. Studart, Bioinspired heart valve prosthesis made by silicone additive manufacturing, Matter 1 (2019) 266–279.
[18] M.G.Ch Nestola, B. Becsek, H. Zolfaghari, et al., An immersed boundary method for fluid–structure interaction based on variational transfer, J. Comput. Phys. 398 (2019).
[19] Ch S. Peskin, The immersed boundary method, Acta Numer. 11 (2002) 479–517.
[20] G.A. Holzapfel, Th C. Gasser, R.W. Ogden, A new constitutive framework for arterial wall mechanics and a comparative study of material models, J. Elast. Phys. Sci. Solids 61 (1) (2000) 1–48.
[21] F. Auricchio, M. Conti, A. Ferrara, S. Morganti, A. Reali, Patient-specific simulation of a stentless aortic valve implant: the impact of fibres on leaflet performance, Comput. Methods Biomech. Biomed. Eng. 17 (3) (2014) 277–285.
[22] A. Gupta, R. Jayaram, A.G. Chaterjee, et al., Energy and enstrophy spectra and fluxes for the inertial-dissipation range of two-dimensional turbulence, Phys. Rev. E 100 (2019).
[23] M. Lesieur, Fourier analysis of homogeneous turbulence, in: Turbulence in Fluids, third ed., Springer Dordrecht, 1997, pp. 155–185.
[24] W. Frost, T.H. Moulden, Spectral theory of turbulence, in: Handbook of Turbulence: Volume 1 - Fundamentals and Applications, Springer New York, 1977, pp. 85–125.
[25] Kitware and Inc., VTK User's Guide, eleventh ed., Kitware Inc., ISBN: 978-1930934238, 2010.
[26] M. Frigo, S.G. Johnson, The design and implementation of FFTW3, Proc. IEEE 93 (2) (2005) 216–231.
[27] A.K.M.F. Hussain, W.C. Reynolds, The mechanics of an organized wave in turbulent shear flow, J. Fluid Mech. 41 (2) (1970) 241–258.
[28] P.A. Davidson, Isotropic turbulence (in spectral space), in: Turbulence: An Introduction for Scientists and Engineers, second ed., Oxford University Press, Great Clarendon Street, 2015, pp. 419–464.
[29] H.K. Moffatt, The degree of knottedness of tangled vortex lines, J. Fluid Mech. 36 (1969) 117–129.
[30] H.K. Moffat, A. Tsinober, Helicity in laminar and turbulent flow, Ann. Rev. Fluid Mech. 24 (1992) 281–312.